Al Haj, Yazan; Mousavihashemi, Seyedabolfazl; Robertson, Daria; Borghei, Maryam; Pääkkönen, Timo; Rojas, Orlando J.; Kontturi, Eero; Kallio, Tanja; Vapaavuori, Jaana

# Biowaste-derived electrode and electrolyte materials for flexible supercapacitors

*Published in:*
Chemical Engineering Journal

*DOI:*
10.1016/j.cej.2022.135058

Published: 01/05/2022

*Document Version*
Publisher's PDF, also known as Version of record

Chemical Engineering Journal 435 (2022) 135058

Contents lists available at ScienceDirect

Chemical Engineering Journal

journal homepage: www.elsevier.com/locate/cej

# Biowaste-derived electrode and electrolyte materials for flexible supercapacitors

Yazan Al Haj [a,1], Seyedabolfazl Mousavihashemi [a,1], Daria Robertson [b], Maryam Borghei [b], Timo Pääkkönen [b], Orlando J. Rojas, PhD [b,c], Eero Kontturi [b], Tanja Kallio [a], Jaana Vapaavuori [a,*]

[a] Department of Chemistry and Materials Science, School of Chemical Engineering, Aalto University, Kemistintie 1, 02150 Espoo, Finland
[b] Department of Bioproducts and Biosystems, School of Chemical Engineering, Aalto University, Vuorimiehentie 1, 02150 Espoo, Finland
[c] Bioproduct Institute, Department of Chemical & Biological Engineering, Department of Chemistry, and Department of Wood Science, The University of British Columbia, 2360 East Mall, Vancouver, BC V6T 1Z3, Canada

ARTICLE INFO

*Keywords:*
Renewable energy
Biowaste-to-energy
Circular economy
Cellulose nanocrystals
Bone-derived porous carbon
Flexible supercapacitors

ABSTRACT

One of the key challenges in the development of energy storage devices relates to material sourcing in harmony with clean technologies. Herein, cellulose nanocrystals (CNC) extracted from brewery residues are used as transparent hydrogel electrolyte after physical cross-linking with aluminum ions ($Al^{3+}$). The hydrogel electrolyte (Al-CNC) exhibits an ultrahigh ionic conductivity (~24.9 mS $cm^{-1}$), high optical transmittance (~92.9% at 550 nm wavelength), outstanding compression strength (3.9 MPa at a 70% strain), and tolerates to various deformations (e.g., twisting, folding, rolling). Meanwhile, animal bone biowaste is used to synthesize porous carbon (PC) electrodes (~879 $m^2$ $g^{-1}$) that are effective in delivering an outstanding specific capacitance (~804 F $g^{-1}$ at 1 A $g^{-1}$). A fully renewable flexible symmetric supercapacitor is assembled by sandwiching the Al-CNC hydrogel between two bone-derived PC electrodes (PC//Al-CNC//PC). The obtained flexible device displays a high energy density (18.2 Wh $kg^{-1}$ at 1 425 W $kg^{-1}$), exceptional power density (20 833 W $kg^{-1}$ at 7.1 Wh $kg^{-1}$), and ~92% capacitance retention after 6 000 cycles at 5 A $g^{-1}$. We further demonstrated the biowaste-derived high-performance flexible supercapacitors for their mechanical durability and reliable electrochemical performance under bending cycles. All combined, the devices are shown to be ideally suited for renewable energy storage applications.

## 1. Introduction

With the rapid advancement of wearable and bendable electronics, there is a growing need for renewable, lightweight, and flexible energy storage devices with high energy and power densities [1–3]. Supercapacitors (SC) have attracted great attention, due to their excellent features including high power density, fast charge–discharge rates, and long cycling lifetime [4–6]. Most commercially available SC use liquid organic electrolytes (for example, tetraethylammonium tetrafluoroborate (TEA-$BF_4$)), which are harmful to the environment and hence not suitable for flexible devices. Moreover, they require appropriate device packaging to prevent electrolyte leakage, hindering any prospects as wearable and bendable electronics [7–9]. To overcome their drawbacks, liquid electrolytes have been replaced with ion conductive gel polymeric electrolytes (GPE), which can also display excellent strength, lightweight, low cost, and relatively easy for manufacturing [10,11]. Compared to solid-state electrolytes, GPE hold liquid electrolytes in the respective matrix, significantly improving ionic conductivity [12,13]. In general, synthetic polymeric networks, such as those produced from polyethylene oxide (PEO) [14], poly(vinyl alcohol) (PVA) [15], and poly(vinylpyrrolidone) (PVP) [15], have been explored as polymer hydrogel electrolytes. Nevertheless, the hydrogel preparation based on petroleum-derived synthetic polymers cannot be considered sustainable option [16]. Therefore, there is a pressing need to develop novel electrolytes based on renewable resources.

Recently, natural polymer-based hydrogels, especially nanocellulose-based hydrogels, have received considerable attention due to their superior properties, sustainability, environmental

* Corresponding author.
*E-mail address:* jaana.vapaavuori@aalto.fi (J. Vapaavuori).
[1] These authors contributed equally to the manuscript.

https://doi.org/10.1016/j.cej.2022.135058
Received 5 November 2021; Received in revised form 22 December 2021; Accepted 31 January 2022
Available online 4 February 2022

handprint, availability, biocompatibility, and low-cost [17,18]. Apart from being the most abundant, renewable, and naturally occurring polysaccharide in the biosphere, cellulose contains abundant hydroxyl groups that makes it easy to functionalize and to act as a host for supramolecular chemistries and to form electrolyte with outstanding properties [18–20]. Extracted from a variety of sources (plants, extracellular domains of bacteria, or tunicates) *via* mechanical and/or chemical treatments, fibers can produce different nanocellulose materials, such as cellulose nanofibers (CNF) and cellulose nanocrystals (CNC), which have distinctive dimensions and structural features [21–23]. Extracted from wide varieties of biowaste materials, food waste and losses (*e.g.*, banana fibers [24,25], potato pulp [26], citrus [27], garlic straw [28], wheat straw [27], and carrot juice residue [29]), nanocellulose has shown interesting trends due to their significant impact if implemented in the circular economy with added benefits of low-cost sourcing [27,30]. In this study, we propose a hydrogel electrolyte from biowaste, with a focus on the extraction of nanocellulose from brewery residues (worldwide annual production of ~39 million tons) [31], from the generation of the fifth most consumed beverage worldwide (~189 billion L in 2018) [32].

In general, cellulose acts as an insulator with low electroactivity, which hinders the application of pure cellulose hydrogel as electrolyte for flexible energy storage devices [33]. Thus, developing novel nanocellulose-based hydrogel with some additives to increase the ionic conductivity and mechanical performance is required. Poosapati *et al.* developed hydrogel electrolyte based on CNF, gelatin, polyacrylic acid (PAA), and potassium hydroxide (KOH) with ionic conductivity of 97 mS $cm^{-1}$ [34]. Chen and coworkers prepared a flexible hydrogel electrolyte adding borax/polyvinyl alcohol (PVA) to CNF hydrogel at around 90 °C, before soaking it in $ZnSO_4$ solution, to exhibit ionic conductivity of 18.1 mS $cm^{-1}$ [35]. Such synthesis protocols involved complex steps, hindering cost-effectiveness and application in modern energy storage devices. Very recently, Yang *et al.* developed a flexible cellulose hydrogel electrolyte using water-in-salt $ZnCl_2$ and $CaCl_2$, in which divalent metal cations ($Zn^{+2}$ and $Ca^{+2}$) crosslinked with the cellulose matrix [12]. The obtained hydrogels showed high ionic conductivity (74.9 mS $cm^{-1}$) and a wide potential window (2.0 V), though ultrahigh concentrations of $ZnCl_2$ (20 M) and $CaCl_2$ (0.5 M) salts were needed to synthesize the hydrogel, increasing the costs and limiting the prospects for mass production [12].

The mechanical properties of the hydrogels are significantly dependent on the added cation charge number [36]. The addition of metal salts with high cation charge numbers ($z > 2+$) as crosslinkers to the nanocellulose matrix may result in hydrogels with superior mechanical properties compared to low charge numbers (mono- or di-valent) used at the same concentration [37]. Therefore, aluminum ions ($Al^{+3}$) are promising as crosslinking agent for the formation of hydrogel electrolytes for energy storage devices with good mechanical strength and ionic conductivity. Al possesses excellent properties such as theoretical specific and volumetric capacity (2 980 mA h $g^{-1}$ and 8 064 mA h $cm^{-3}$, respectively) [38] and low cost (1 885 USD/ton) [39] compared to Zn (820 mA h $g^{-1}$, 5 855 mA h $cm^{-3}$, and 2 573 USD/ton, respectively) [40] and many other metals [39]. To the best of our knowledge, while all-nanocellulose hydrogel electrolytes have been mostly based on CNF, no systematic studies have focused on CNC as a host for such hydrogels. Despite the lower aspect ratio of CNC compared to CNF the need for additional processing steps to form hydrogels, CNC hydrogels are proposed for their improved colloidal stability, mechanical properties, and higher tendency to align under shear [41]. It is worth mentioning that the majority of CNC reported in literature are prepared by sulfuric acid and therefore contain sulfate groups which impart colloidal stability to the CNC [41]. By contrast, we are using HCl hydrolysis coupled with TEMPO-oxidation which results in carboxylates on CNC surface (instead of sulfates), in which the charge density of the carboxylates is much higher than that of sulfates. The high charge density causes gelling of the CNC dispersion at far lower concentrations (~1 wt%) than with sulphated CNC (>10 wt%) [41].

According to $E = 0.5CV^2$, the energy density of SC is directly proportional to its capacitance as well as the square of the operating potential window of the electrolyte [5]. Thus, the electrochemical performance of SC is not only determinant by the electrolyte, but also by the electrode materials properties (e.g., electrical conductivity, specific surface area, and structure porosity). Metal oxides/chalcogenide-based SC exhibit high specific capacitance, but they suffer from poor cyclic life compared to carbonaceous materials. Among carbonaceous electrode materials, active carbon has been widely used in commercial SC, because of its superior properties including large specific surface area (~1500 $m^2$ $g^{-1}$), good electrical conductivity, and moderate synthesis cost. Due to the microporosity (<0.4 nm) of active carbon compared to the electrolyte ions (0.6–0.76 nm), it possesses poor ion transport/adsorption, which results in low specific capacitance (<200 F $g^{-1}$), poor power and energy densities (<8 Wh $kg^{-1}$) [42]. Such drawbacks can be solved by the synthesis of porous carbon (PC) materials sourced from biowaste (eggshells [43], soybean dregs [44], ant powder [45], ground cherry calyces [46], and corncob [47,48]), not only because they are cost-effective and eco-friendly, but they also provide appropriate pore size distribution for ion mobilities as well as excellent network for heteroatom dopants (N, O, P, and S). Animal bone is another biowaste produced in large quantities. It is one of the most promising materials for energy applications because it contains high concentrations of P, Ca, S, and N, making it an attractive source of heteroatoms for preparation of *in-situ* doped PC materials [49].

Herein, we demonstrate for the first time, the preparation of flexible symmetric SC derived from biowastes, composed of a 3D CNC hydrogel electrolyte and PC electrode materials. After the isolation of CNC from brewery residues, the hydrogel electrolyte was prepared by a facile and cost-effective single-step method, *via* physically cross-linking the carboxylate surface groups of the CNC with a high valency cation ($Al^{+3}$), without any external energy sources (mechanical or thermal). The cross-linked hydrogel electrolyte (Al-CNC) showed high electrical conductivity, optical transparency, and mechanical properties. As electrode materials, we fabricated a PC 3D network derived from animal bones, which displayed large specific surface area and excellent porous network. The assembled PC//Al-CNC//PC symmetric flexible SC showed outstanding electrochemical performance and mechanical durability at different bending angles. The results exhibit the promising potential of biowaste-derived materials in next-generation flexible energy applications.

## 2. Materials and methods

### 2.1. Materials

Commercial barley malt (Viking Malt Pilsner EBC 3) was used as a source of carboxylated CNC. Sodium hydroxide (NaOH) and sodium hypochlorite (NaOCl) were obtained from VWR (USA). HCl gas (99.8%) was purchased from AGA (Sweden). Sodium chlorite ($NaClO_2$), sulfuric acid ($H_2SO_4$), hydrochloric acid (HCl), 2,2,6,6-tetramethylpiperinide-1-oxyl radical (TEMPO), and aluminum nitrate ($Al(NO_3)_3$) were purchased from Sigma-Aldrich (Germany). All chemicals were used without further purification. Commercial Solabiol bone granules (branded as natural fertilizer) were used to produce the porous carbon.

### 2.2. Production of carboxylated CNC from beer residues

The barley malt Viking Malt Pilsner EBC 3 was mashed and dried after removal of wort. Beer residues were alkali-extracted with 2 M NaOH (2 h, 85 °C) and washed thoroughly with water. Then, fibers were acid hydrolyzed with HCl gas following a novel hydrolysis system, as previously reported [50]. Fibers were washed with water after acid hydrolysis. The collected fibers were TEMPO-oxidized with bromide-free process [51]. Carboxylated CNC were produced to 1.0 wt%

dispersion according to the process reported with bacterial cellulose [21]. The obtained CNC possessed a charged density of 1.25 ± 0.02 mmol COOH groups per gram.

### 2.3. Preparation of the Al-CNC hydrogel

3 mL of CNC suspension (1.0 wt%) was first sonicated for 10 mins and then poured into a silicon mold (4 × 2 × 2 $cm^3$, purchased from AliExpress). Then, 3 mL of 4 M of $Al(NO_3)_3$ was added dropwise, against the wall of the mold, to the previous suspension. After 24 h of cross-linking, the obtained hydrogel was washed by DI water several times to remove unreacted salt traces. The obtained hydrogel electrolyte was designated as "Al-CNC". For electrochemical measurements comparison, 4 M $Al(NO_3)_3$ liquid electrolyte was prepared without the addition of CNC, and designated as "Al-LE".

### 2.4. Preparation of bone-derived PC

The bone granules were crushed with a paddle blade and dried at 105 °C overnight. The bone powder was placed uniformly in a ceramic crucible and carbonized in a horizontal tube furnace (NBD-O1200-50IC) at 900 °C for 2 h with 5 °C $min^{-1}$ ramp rate under $N_2$ atmosphere. The obtained carbon was leached with 1 M HCl and washed with deionized water until neutral pH. The obtained PC was dried at 105 °C overnight and ground with a mortar. Then, a second carbonization step was performed at 900 °C for 1 h (ramp rate of 5 °C $min^{-1}$).

### 2.5. Material characterizations

#### 2.5.1. Attenuated total reflection fourier transform infrared (ATR-FTIR) spectroscopy

The metal carboxylate structures in the obtained Al-CNC were analyzed using ATR-FTIR spectrometer (Spectrum Two FT-IR Spectrometer, PerkinElmer, USA) after the lyophilization (freeze-drying) of the hydrogel. ATR measurements were conducted using diamond crystal as the internal reflection element. The spectra were recorded at wavenumber range of 500–4000 $cm^{-1}$ with accumulation of 24 scans and a resolution of 2 $cm^{-1}$. ATR-FTIR spectra of pristine CNC was also measured for comparison.

#### 2.5.2. Ultraviolet–visible (UV–Vis) spectroscopy

The optical properties of Al-CNC were investigated by measuring the total transmittance using UV–Vis spectroscopy (Shimadzu UV-2600 spectrometer, Shimadzu Co. Japan) with a wavelength range from 200 nm to 900 nm.

#### 2.5.3. Mechanical performance

The compressive stress–strain measurements of the Al-CNC hydrogel were investigated using Instron 4204 Universal Testing fitted with a 1 kN load cell. The hydrogel was prepared in a cylindrical shape using a custom-made Teflon mold with a diameter of 18 mm and thickness of 10 mm. The compression was done to 70% of the original thickness of the Al-CNC hydrogel at a compression speed of 3 mm $min^{-1}$ at room temperature. The mechanical testing was examined and averaged on four replicates.

#### 2.5.4. Scanning electron microscopy (SEM)

The morphology of the obtained Al-CNC hydrogel and PC were observed using scanning electron microscopy (SEM, Tescan MIRA 3, Brno, Czech Republic) with an acceleration voltage of 3.0 and 5.0 kV, respectively. Before observation the Al-CNC hydrogel was first freeze-dried and then coated with 5 nm gold–palladium (Au-Pd) layer. Both materials (freeze-dried Al-CNC and PC) were deposited on a double side carbon tape and then air was blown at them to remove any loose particles. This will prevent them from detaching within the apparatus in a vacuum.

#### 2.5.5. Raman spectroscopy

Renishaw 1000 UV was used for Raman spectroscopy. The equipment used for the measurements contained 532 nm diode laser, an air-cooled CCD detector, and 2 gratings. The spectral collection 35 integration times for one acquisition were 20 s. The confocal aperture of 50 mm was used during the measurements. The laser power was chosen to be 10 mW at the sample surface.

#### 2.5.6. Nitrogen sorption isotherms

Micromeritics TriStar II 3020 equipped with an automated surface area and pore size analyzer was used to measure $N_2$ adsorption–desorption in porous carbons at 77 K. Prior to the measurements, about 10 mg of the samples were placed in sample cell and left in a degas system (Micromeritics II, Flow Prep 060) at 105 °C for 5 h under $N_2$ flow. The Brunauer-Emmett-Teller (BET) method was used to determine the specific surface area, while Barrett-Joyner-Halenda (BJH) method and DFT were applied to obtain the pore volume and pore size distributions.

#### 2.5.7. X-ray photoelectron spectroscopy (XPS)

Surface chemical analysis of the porous carbons were performed using X-ray photoelectron spectroscopy (XPS) containing AXIS Ultra electron spectrometer (Kratos Analytical, UK) with monochromatic Al Kα irradiation (incident energy = 1486.6 eV). An 80 eV pass energy was used for survey spectra. The measurements were done at 90° angle under ultra-high vacuum. A neutralizer was used to avoid charging effects. The spot size for these measurements was around 1 mm diameter and the area analyzed of 300 μm × 700 μm.

### 2.6. Electrochemical measurements

#### 2.6.1. PC ink preparation:

Electrode inks were prepared by dispersing 10 mg of the porous carbon in 950 μL ethanol. After 1 h stirring, 50 μL of Fumion® (10% FAA3 ionomer in N-Methylpyrrolidone) was added and immediately sonicated for 10 min, and then was left on magnet stirring overnight. Right before the application, the ink was sonicated again for 10 min.

#### 2.6.2. Measurements in three-electrode systems

Electrochemical evaluation of PC and Al-CNC was performed in three-electrode (half-cell) and two-electrode (full cell) assemblies. First, three-electrode system measurements were performed. Glassy carbon (GC) with 5 mm diameter was used as working electrode. 1 μL of PC ink was drop-casted on GC and dried at 80 °C for 30 min. This sample was labelled as "PC". The active material loading on GC electrode was 0.051 mg $cm^{-2}$. Ag/AgCl in saturated KCl and Pt mesh with high surface area were used as reference and counter electrodes, respectively. The electrodes were soaked in 4 M $Al(NO_3)_3$ aqueous solution, as liquid electrolyte (Al-LE), for electrochemical characterizations. To compare liquid and hydrogel electrolytes, a 2-mm thick piece of hydrogel was cut and placed between working and counter electrodes. Reference electrode was placed close to working electrode, as shown in **Figure S1**. The three electrode measurements were conducted by using a Autolab potentiostat (PGSTAT128N). The working electrodes were first cycled by cyclic voltammetry (CV) at a scan rate of 50 mV $s^{-1}$ to stabilize the cell and then CV measurement of the electrodes were conducted over a voltage range from −0.3 to 0.7 V vs. Ag/AgCl at different scan rates (i.e., 10, 25, 50, 100, 200 mV $s^{-1}$). Electrochemical impedance spectroscopy (EIS) measurements were conducted in frequency range of 100 kHz to 15 mHz. 5 mV voltage amplitude at OCP was applied to excite the working electrode.

#### 2.6.3. Measurements of flexible supercapacitor

Full cell assembly of the supercapacitor was assembled by casting PC ink on two strips (5 mm × 70 mm) of gas diffusion layer (GDL, FuelCellsEtc® GDLCT) and packing electrodes with a layer of hydrogel (5 mm width × 20 mm length × 2 mm thickness) in between. It is worth

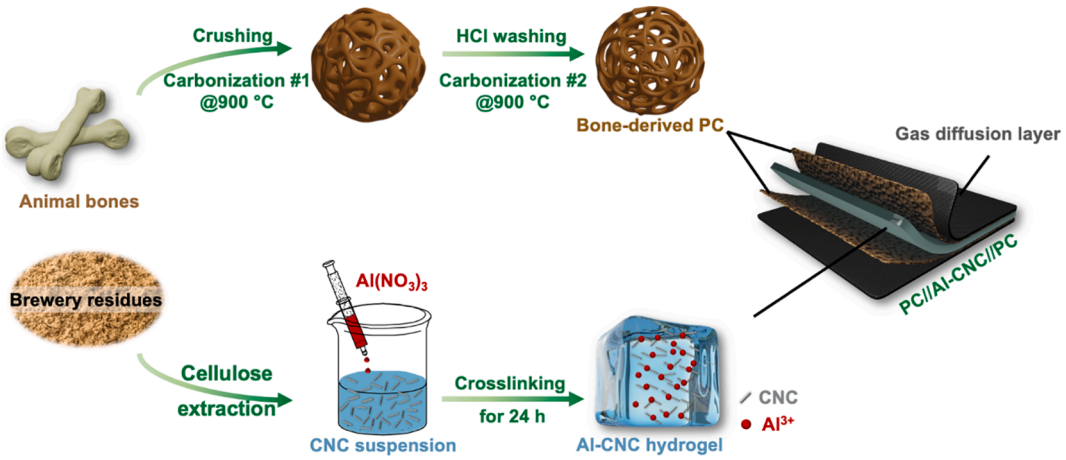


**Fig. 1.** Schematic illustration for the synthesis of Al-CNC and PC to assemble the flexible supercapacitor (PC//Al-CNC//PC).

mentioning that GDL is made of woven carbon-cloth treated with PTFE, which is not considered as environmentally hazardous material according to Chemical Hazard Information and Packaging (CHIP) regulations. The assembly was wrapped by a Teflon tape to prevent water evaporation. The flexible supercapacitor electrochemical tests were performed using BioLogic® (MPG-205). Full cells were galvanostatically cycled at 5 A $g^{-1}$ current density after CV and EIS measurements. The flexibility of the symmetric supercapacitor was also examined at a bending angle of 90°. The specific capacitance of active material was obtained from CV using equation (1):

$$SC = \frac{\int IdV}{2m\nu\Delta V} \tag{1}$$

where, $\int IdV$, $m$, $\nu$ and $\Delta V$ are obtained surface area from voltammogram (A.V), mass of the active material (g), scan rate (V $s^{-1}$) and potential window (V), respectively.

The capacitance of electrodes was calculated based on equation (2) from galvanostatic charge–discharge (GCD) measurements:

$$SC = \frac{It_{discharge}}{\Delta V} \tag{2}$$

where, $I$, $t_{discharge}$, and $\Delta V$ are current (A), discharge time (s) and potential window (V), respectively. GCD tests were performed at different current densities of 2.5, 5, 10, 25 and 50 A $g^{-1}$ to evaluate the rate capability of active materials. Energy density was calculated by integrating the area under discharge curve during GCD cycling at different current densities (equation (3)):

$$E_D = \int_0^{t_d} \frac{VIdt}{3600.m} \tag{3}$$

The power density of the device at different current densities was calculated using equation (4):

$$P_D = \frac{V_0^2}{4R_{ES}m} \tag{4}$$

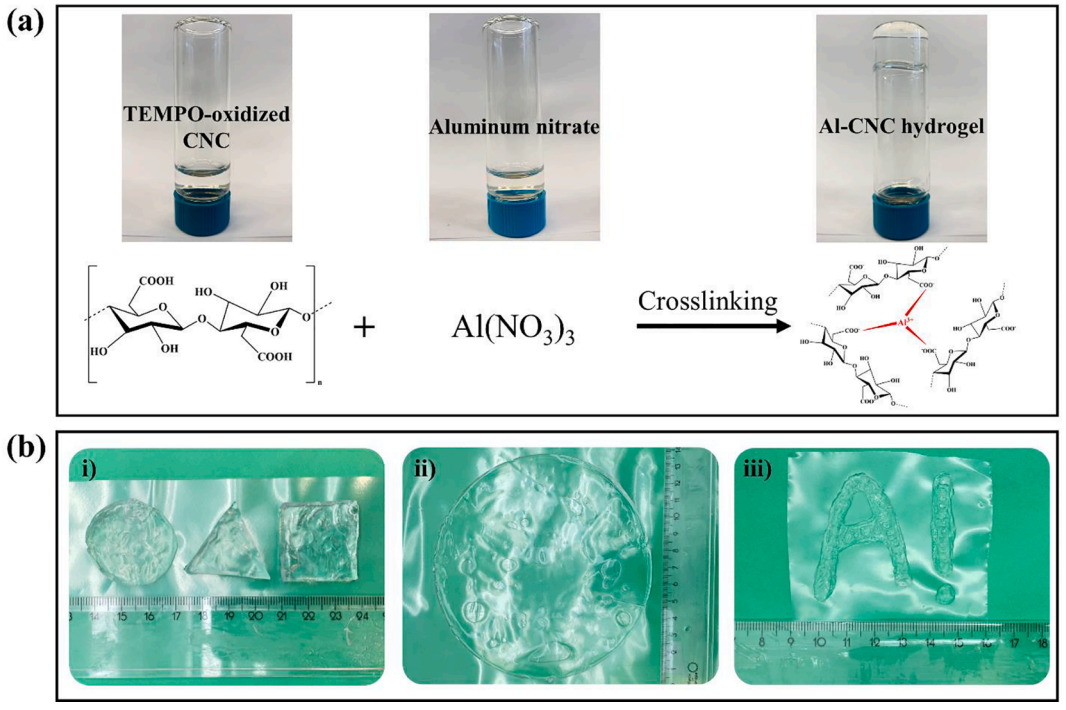


**Fig. 2.** (a) The chemical reaction between TEMPO-oxidized CNC and $Al(NO_3)_3$; (b) Al-CNC hydrogels i) different geometries, ii) larger dimensions, and iii) manual printing (Aalto University logo).

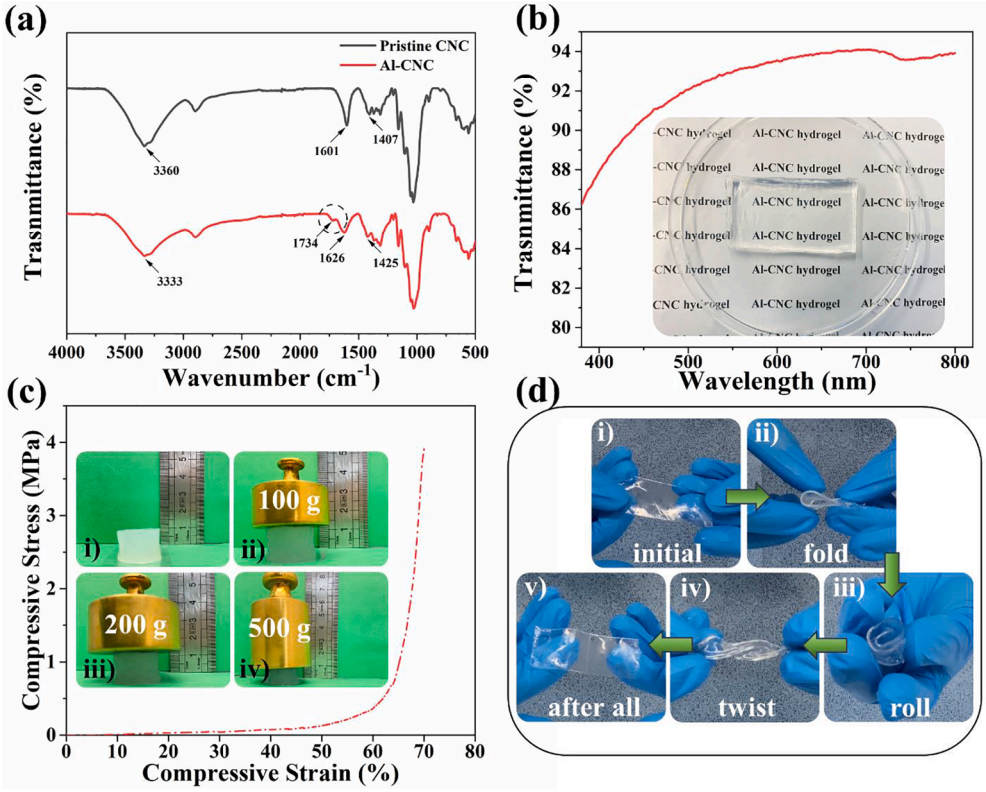


**Fig. 3.** (a) FT-IR spectra of pristine CNC and Al-CNC; (b) Total transmittance as a function of wavelength (380–800 nm) for Al-CNC (inset is a photograph of the Al-CNC hydrogel); c) Compressive stress–strain for Al-CNC hydrogel (inset photographs of Al-CNC hydrogel with different loads i) no load; ii) 100 g; iii) 200 g; and iv) 500 g); and (d) Photographs of Al-CNC hydrogel under various deformations i) initial, ii) folding, iii) rolling, iv) twisting, and v) recovering.

where, $V_0$ is the potential window of the device and $R_{ES}$ is the equivalent series resistance ($\Delta V/\Delta I$, values obtained from ohmic drop of the galvanostatic discharge profile), $m$ is the mass of the electrode loading (g). Columbic efficiency (CE) of the GCD cycling was calculated by dividing the capacity of discharge to the capacity of the charge in every cycle.

$$CE = \frac{C_{dis}}{C_{cha}} \tag{5}$$

## 3. Results and discussion

The synthesis of Al-CNC as hydrogel electrolyte and PC as electrode materials is displayed in Fig. 1. First, the brewery residues were converted into a CNC suspension, which was added into a silicon mold before the addition of $Al(NO_3)_3$ to induce physical cross-linking (Fig. 2**a**). Al-CNC can also be fabricated in different geometries, dimensions, and by manual printing, as displayed in Fig. 2**b**. The PC was prepared from animal bones after carbonization followed by acid (HCl) washing.

Chemical and optical characterization

The intermolecular interactions after the physical crosslinking between the $Al(NO_3)_3$ and nanocellulose matrix in the lyophilized hydrogel was examined by FT-IR spectroscopy, Fig. 3**a**. The FT-IR spectra of pristine CNC includes a broad absorption peak at 3360 $cm^{-1}$, corresponding to the O−H stretching vibration. The peaks located at a wavenumber of 1601 and 1407 $cm^{-1}$ can be assigned to carbonyl bond (−C=O stretching vibration) and O−H bending, respectively [52]. However, after the addition of $Al(NO_3)_3$, some changes were clearly observed in the spectrum of Al-CNC (Fig. 3**a**). Both adsorption peaks of −C=O stretching, and O−H bending shifted towards higher wavenumbers, from 1601 to 1626 $cm^{-1}$ and from 1407 to 1425 $cm^{-1}$, respectively, and towards lower wavenumbers for O−H stretching peak (from 3360 to 3333 $cm^{-1}$). In addition, an extra peak at 1734 $cm^{-1}$ which corresponds to the coordination between $Al^{3+}$ and carboxylic groups was observed [53]. All the aforementioned changes confirm the intermolecular electrostatic interactions and compatibility between the oxidized nanocellulose and $Al^{3+}$ to form a cross-linked network.

The transmittance of the Al-CNC was examined using UV–Vis spectrometer at a wavelength range of 380–800 nm (Fig. 3**b**). As shown in the spectra, the transmittance of the Al-CNC hydrogel (thickness of 5 mm) was > 86% throughout the visible spectrum, and approximately 92.9% at 550 nm wavelength. The absence of scattering in the UV–Vis spectrum of Al-CNC hydrogel confirms the excellent homogeneity and physical cross-linking between the aluminum ions ($Al^{3+}$) and the cellulose matrix, which possesses a promising potential as a novel electrolyte for transparent electronics and energy storage devices [65][54].

Morphology and Mechanical Performance

Desirable mechanical properties are significant for flexible hydrogel electrolytes because they play a role as electrolyte and a separator sandwiched between the electrodes, *e.g.*, in the supercapacitor assembling process. The compressive stress–strain curve for Al-CNC hydrogel with a thickness of 10 mm and diameter of 18 mm is shown in Fig. 3**c**. The hydrogel exhibited excellent mechanical properties without failure, with a compressive stress of approximately 3.9 MPa at a compression rate of 70% (Fig. 3**c**). The inset photographs (Fig. 3**c** i-iv) display the changes in height of the Al-CNC at different loads (100, 200, and 500 g). The results indicate the formation of a network structure with outstanding mechanical strength via a single-step physical crosslinking process in comparison with recent literature (**Table S1**). Fig. 3**d** depicts that Al-CNC hydrogel can be easily folded, rolled, and twisted without any obvious cracks, demonstrating its outstanding mechanical properties for flexible energy storage devices.

The morphology of the lyophilized Al-CNC was analyzed by SEM, as shown in Fig. 4**a and b**. The SEM images show how the compact 3D

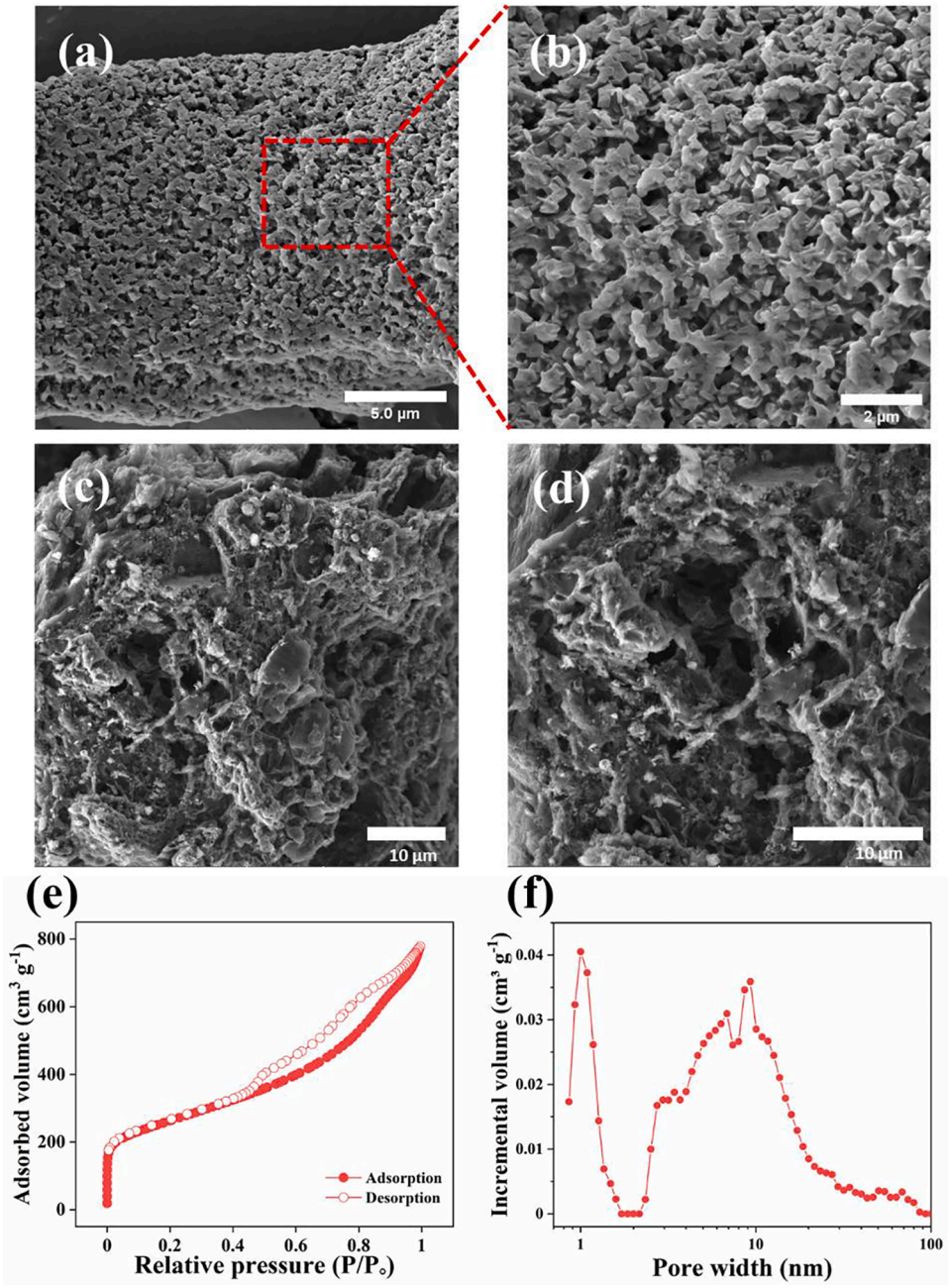


**Fig. 4.** Structural characterization. SEM images of (a-b) freeze-dried Al-CNC (c-d) PC at low and high magnifications, respectively; (e) N2 adsorption–desorption spectra; and (f) Pore size distribution from DFT method.

network was converted into a highly porous structure after lyophilization. Such architectures possess high mechanical strength, which is consistent with the observed mechanical properties of the Al-CNC hydrogel. Moreover, the porous structure improves the transportation of ion carriers through the hydrogel electrolyte; the hierarchical structure offers ion-transport pathways with minimized diffusion distance and resistance, which significantly enhances the overall performance of the supercapacitor [55]. The morphology of the bone-derived carbon is presented in SEM micrographs (Fig. 4**c and d**). It can be observed that the fibrillar structure of the collagen fibers remained after carbonization. Meanwhile, acid washing leached the minerals and produced pores among collagen fibers with open hierarchical structure, resulting in the shortening of ion/electron transport pathways, therefore improving the electrochemical performance [5].

Nitrogen sorption isotherms

The $N_2$ adsorption isotherms and the pore distribution of bone-derived carbon are illustrated in Fig. 4**e and f**. A type IV isotherm with a hysteresis loop at relative pressure >0.4 indicated a dominant mesoporous structure [56]. The low-pressure region of the isotherm relates to the micropore filling, while the plateau at high relative pressures corresponds to the multilayer adsorption in the meso- and macropores. The specific surface area obtained by the BET method was 879 $m^2\ g^{-1}$, and the results included a large pore volume of 1.14 $cm^3\ g^{-1}$. The pore size distribution showed a sharp peak at ~1 nm, followed by wide distribution of mesopores from 2 to 100 nm, indicating a hierarchical porous structure (Fig. 4**f**). The large specific surface area and the highly porous nanostructure may be advantageous as ion/electron pathway and to improve the electrochemical properties of bone-derived PC [57].

Raman and XPS

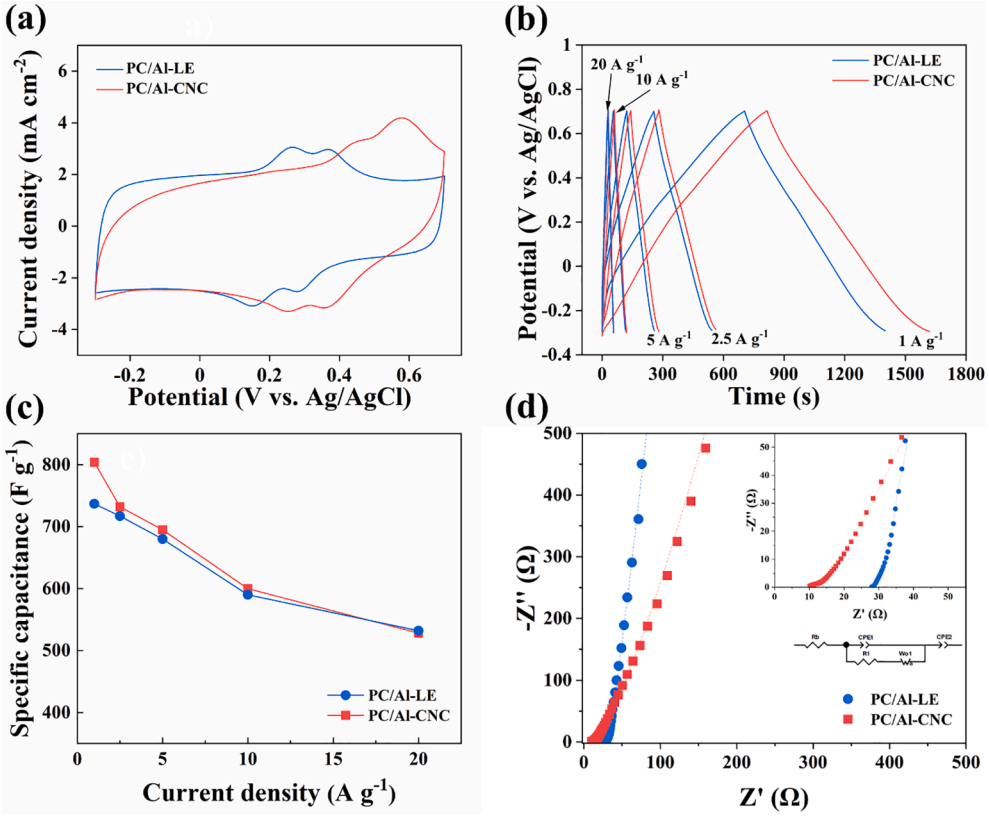


**Fig. 5.** Electrochemical evaluation of PC/Al-CNC compared to PC/Al-LE electrolyte by (a) CV at a scan rate of 50 mV $s^{-1}$; (b) GCD at different current densities (from 1 to 20 A $g^{-1}$); (c) Rate capability; and (d) EIS spectrum (inset displays the equivalent circuit).

The Raman spectrum of the bone-derived carbon (Figure S2) shows a D-band (at 1351 $cm^{-1}$) and a G-band (at 1581 $cm^{-1}$), which are characteristics of the $sp^3$ defects in carbon aromatic rings, and $sp^2$-bond graphitic carbons, respectively [58]. The ratio of $I_D$ to $I_G$ (0.94) presents more ordered structures compared to the bone-derived carbon obtained at 850 °C ($I_D/I_G$: 1.007) by Wang et al. [59] likely because of higher pyrolysis temperature (at 900 °C) and the second step of carbonization at 900 °C, after leaching the minerals by hydrochloric acid.

The XPS spectra of the carbon samples (Figure S3) depicts a strong carbon C1 s peak at 284.3 eV, signals for oxygen (O1 s at around 532 eV) as well as nitrogen N1 s ca. 400 eV. The oxygen atomic content and nitrogen atomic content are about 5.9% and 2.1%, respectively. The significant content of nitrogen indicates the *in-situ* doping of the carbon occurred by decomposition of collagen, and agrees with the values (2.27%) reported by Niu et al. [58].

Electrochemical evaluation

*Electrochemical measurements of three-electrode system*

The electrochemical performances of the obtained materials were evaluated in a typical three-electrode system by CV, GCD, and EIS (Fig. 5); where PC drop-casted on GC as the working electrode, Al-CNC hydrogel as the electrolyte, Ag/AgCl as the reference electrode, and Pt mesh as the counter electrode. Figure S4**a** depicts the ultralow current density of bare GC in both electrolytes in comparison to their counterparts (PC/Al-LE and PC/Al-CNC), which indicates the negligible influence on the capacitive properties of the active material under the same electrochemical measurements. To evaluate the superior performance of the Al-CNC hydrogel electrolyte, a comparative three-electrode system using Al-LE was examined by CV at a scan rate of 50 mV $s^{-1}$ with an operating potential window from −0.3 to 0.7 V vs Ag/AgCl, as shown in Fig. 5**a**. The current density was normalized by glassy carbon electrode area. The voltammograms of the PC electrode in both liquid and hydrogel electrolytes showed the pseudocapacitive nature of the electrode. However, the Al-CNC hydrogel exhibited higher current density compared to the Al-LE in both comparisons (PC and bare GC), demonstrating that hydrogel electrolyte has higher ionic conductivity compared to its counterparts. It is noticeable that PC/Al-LE shows double redox peaks (at around 0.26 and 0.37 V vs Ag/AgCl for oxidation and 0.15 and 0.28 V vs. Ag/AgCl for reduction). The double peaks are shifted 200 mV towards positive voltages in hydrogel electrolyte. These peaks indicate the presence of $Al^{3+}$ intercalation in the porous carbon structure [60]. Figure S4**b** displays the CV curves of PC/Al-CNC at various scan rates from 10 to 200 mV $s^{-1}$. It was observed that the peak current density enormously increases as the scan rate increased, while the shape of CV is maintained showing outstanding rate performance of the PC/Al-CNC. It should be noted that in these results the synergistic effect of intercalation features (redox peaks) with double layer capacity may affect the voltammogram shape which is shown in Figure S4**b** [61]. It was also observed that increasing scan rate causes oxidation and reduction peaks to shift slightly towards positive and negative potentials, respectively. This is due to the effect of the scan rate on the thickness of the diffusion layer on the electrode surface. At higher scan rates, ions tend to transfer faster, thus the shape of the voltammogram will be affected. For comparison, the CV curves of PC/Al-LE at various scan rates (10 to 200 mV $s^{-1}$) are presented in Figure S4**c**.

The GCD curves of the PC/Al-CNC and PC/AL-LE at various current densities ranging from 1 to 20 A $g^{-1}$ within an operating potential window of −0.3 to 0.7 V vs Ag/AgCl are displayed in Fig. 5**b**. In the case of PC/Al-CNC, the GCD curves showed pseudocapacitive behavior, high symmetric characteristics. Furthermore, no obvious IR drop was observed, indicating that PC electrode possess ultrahigh Coulombic efficiency (CE) and rate capability, which is in a good agreement with CV studies. At a current density of 1 A $g^{-1}$, the PC/Al-CNC possess higher discharging time (~804 s) compared to PC/Al-LE (~695 s), as presented in Figure S5. Based on the GCD characteristics, the specific capacitance

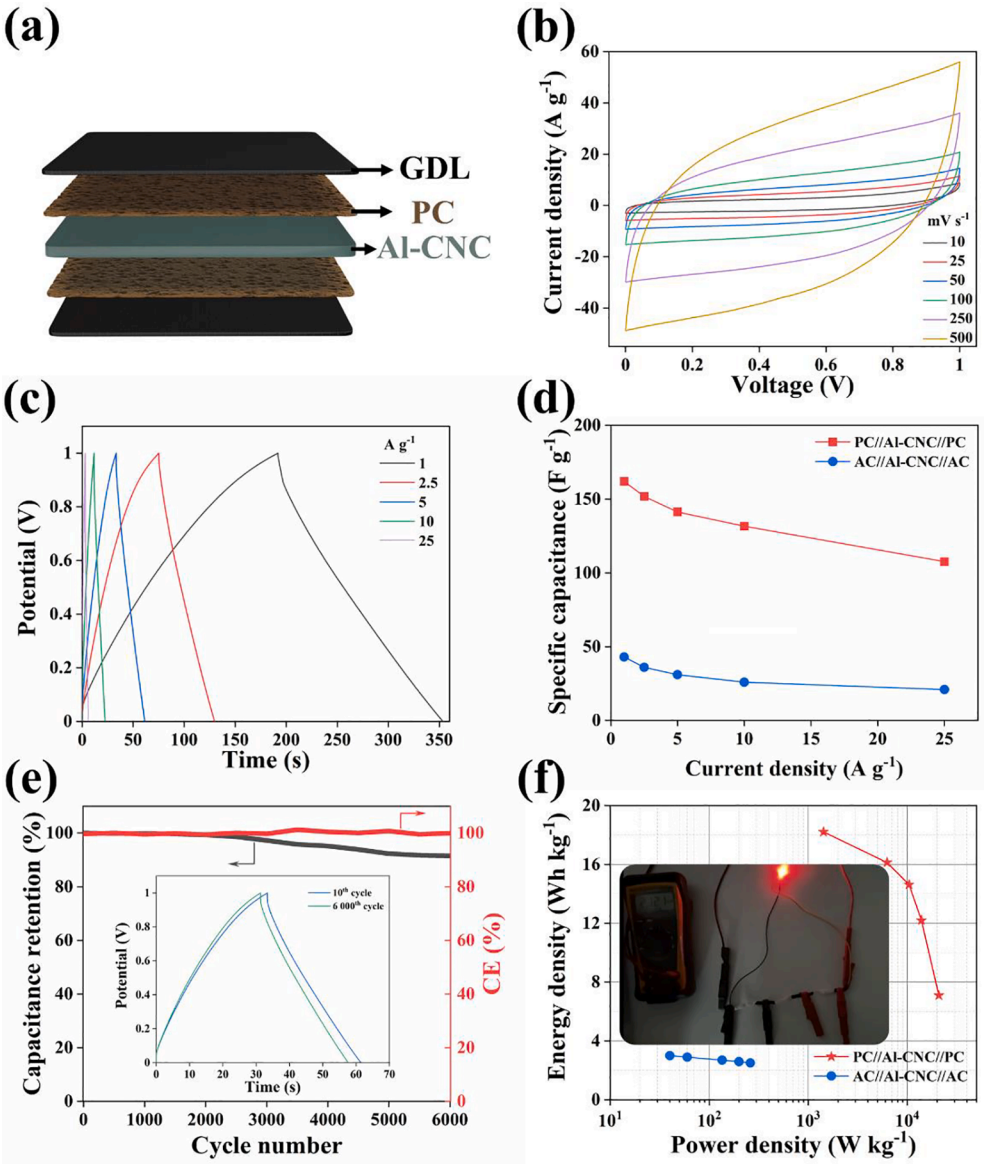


**Fig. 6.** Electrochemical performance of PC//Al-CNC//PC supercapacitor device: (a) Schematic structure of the assembled symmetric supercapacitor; (b) CV at different scan rates (from 10 to 500 mV $s^{-1}$); (c) GCD at different current densities (from 1 to 25 A $g^{-1}$); (d) Specific capacitance vs. current density of PC//Al-CNC//PC and AC//Al-CNC//AC; (e) Cycling performance and Coulombic efficiency of PC//Al-CNC//PC at a current density of 5 A $g^{-1}$ after 6 000 consecutive charge–discharge cycles (inset shows the corresponding GCD curves of 10th and 6 000th cycles); and (f) Ragone plot comparison between PC//Al-CNC//PC AC//Al-CNC//AC (inset displays a glowing red LED).

was calculated and presented in Fig. 5**c**. The PC/Al-CNC exhibited a specific capacitance of around 804 F $g^{-1}$ at a current density of 1 A $g^{-1}$, which is superior compared to PC/Al-LE (737 F $g^{-1}$) at the same current density. As the current density increases from 1 to 20 A $g^{-1}$, the specific capacitance of both three-electrode systems decreases. The PC/Al-CNC exhibited specific capacitance as high as 804, 732, 695, 600, and 528 F $g^{-1}$ at current densities of 1, 2.5, 5, 10, and 20 A $g^{-1}$, respectively. At the same current densities PC/Al-LE exhibited a specific capacitance of 737, 717, 680, 590, 532 F $g^{-1}$, respectively. Even at high current density at 20 A $g^{-1}$, around 65.7% of initial specific capacitance was retained for PC/Al-CNC and 72.1% for PC/Al-LE (Fig. 5**c**). The areal capacity for PC/Al-CNC and PC/Al-LE were also calculated and presented in **Table S2**. Such results also confirm that the 3D network of the hydrogel electrolyte plays a significant role in improving the specific capacitance of the device in comparison to its counterparts [62]. It also confirms that the bone-derived PC exhibits extraordinary specific capacitance in both electrolytes and overall electrochemical performance in comparison with previously reported biowaste-derived carbon-based materials (**Table S3**).

The EIS analysis is one of the most significant techniques to study the charge transfer kinetics of electrode materials. Fig. 5**d** shows the Nyquist plots related to the PC electrode in liquid and hydrogel electrolytes. The EIS results for both electrolytes were fitted with the same equivalent circuit (EC, inset circuit in Fig. 5**d**). $R_b$ and $R_1$ were assigned to the resistance of the electrolyte and charge transfer resistance, respectively. CPE1, Wo1, and CPE2 were assigned to (de-)intercalation of ions into porous structure, diffusion of ions in electrolyte, and double layer capacitance, respectively. Fitting the experimental data obtained from EIS was done using Z-View® software and the data is presented in **Table S4**. The EIS results were in good agreement with the CV characteristics in which a redox phenomenon is combined with double layer charge storage. Bulk resistance ($R_b$) of the electrolyte is lower for hydrogel (9.49 Ω) compared to the Al-LE (27.75 Ω), indicating more conducting nature of hydrogel electrolyte. Ions (de-)intercalation resistance ($R_1$) is 6.88 and 4.66 Ω for liquid and hydrogel electrolytes, respectively. These values are very close, and it can be concluded that the gel electrolyte has successfully wetted the porous material. Double layer capacity (CPE2-T) values for Al-CNC (0.0084F.$s^{(1-n2)}$) and Al-LE (0.0071F.$s^{(1-n2)}$) confirm the results obtained from CV related to capacitance. In addition, the ionic conductivity of the Al-CNC hydrogel was also examined by sandwiching a 5 mm thick hydrogel between two stainless steel plates (**Figure S6**). The Al-CNC showed an ionic

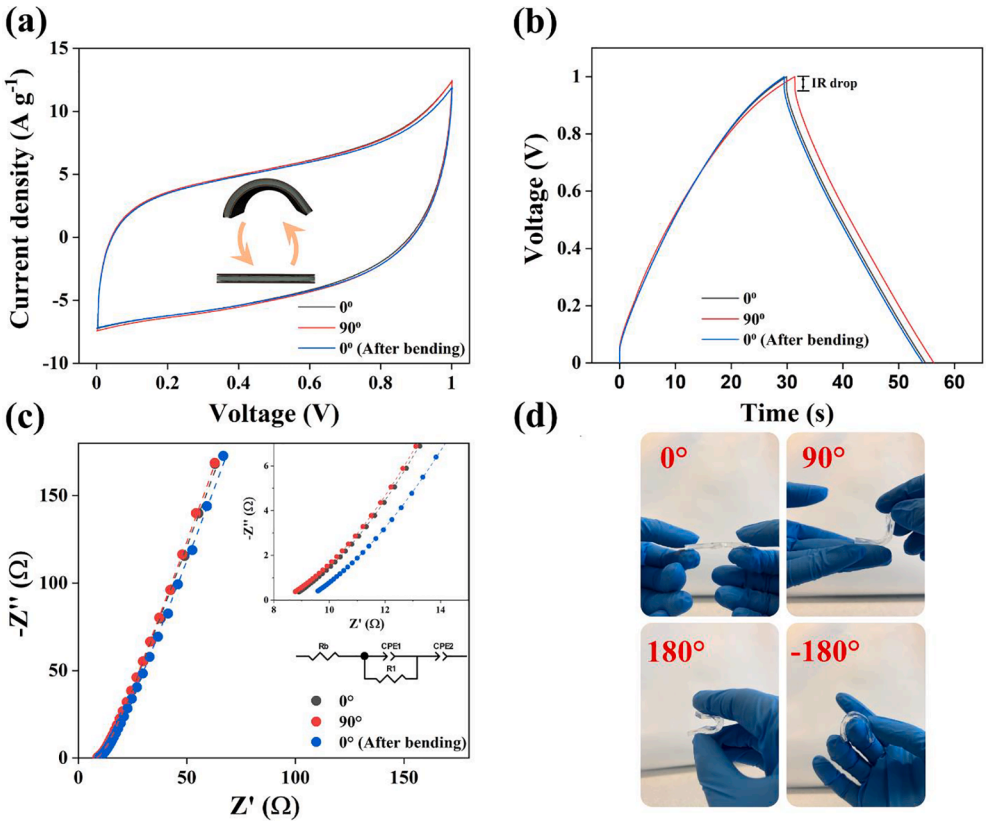


**Fig. 7.** The effect of bending on the electrochemical performance of the cell: (a) CV at a scan rate of 50 mV $s^{-1}$; (b) GCD at a current density of 5 A $g^{-1}$; (c) EIS (inset shows the EC model); and (d) Photographs of Al-CNC hydrogel at various bending angles (0°, 90°, 180°, and −180°).

conductivity as high as 24.9 mS $cm^{-1}$, which is superior to previously reported hydrogel electrolytes, as shown in **Table S1**.

*Electrochemical measurements of two-electrode system*

Flexible symmetric supercapacitor was constructed by using bone-derived PC as positive and negative electrode as well as Al-CNC hydrogel as the electrolyte (PC//Al-CNC//PC), as displayed in Fig. 6**a**. The CV curves of PC//Al-CNC//PC supercapacitor at various scan rates ranging from 10 to 500 mV $s^{-1}$ with an operating potential window from 0 to 1.0 V are depicted in Fig. 6**b**. All CV curves of the device demonstrate a slightly deformed rectangular shape which shows the coexistence of double layer capacitor and pseudocapacitive performance [63]. The absence of the redox peaks in all CV curves indicate that the SC are charged and discharged at a constant pseudo-constant rate over the entire voltammetric cycles [64].

The shape of CV curves was maintained at very high scan rates (500 mV $s^{-1}$), which indicates the high-rate performance of the supercapacitor. Fig. 6**c** exhibits the GCD profile of the PC//Al-CNC//PC supercapacitor at different current densities ranging from 1 to 25 A $g^{-1}$ with an operating potential window of 0 to 1.0 V. The GCD results were also in good agreement with cyclic voltammograms indicating high capacitance provided by double layer capacitor and less pseudocapacitive behavior. The calculated specific capacitances of PC//Al-CNC//PC are as high as ~162, 152, 141, 132, and 107 F $g^{-1}$ at current densities of 1, 2.5, 5, 10, and 25 A $g^{-1}$, respectively (Fig. 6**d**). As the current density increased from 1 to 25 A $g^{-1}$ the specific capacitance of the PC//Al-CNC//PC supercapacitor has slightly decreased from 162 to 107 (~66% capacitance retention), which could be due to the increase in voltage drop. The PC//Al-CNC//PC supercapacitor retained 48.8% of its initial specific capacitance (43 F $g^{-1}$) at a high current density of 25 A $g^{-1}$ (Fig. 6**d**). The PC//Al-CNC//PC supercapacitor exhibits a superior electrochemical performance in comparison to AC//Al-CNC//AC as well as previously reported biowaste-derived SC, as shown in **Table S5**.

One of the most critical parameters that hinder the overall electrochemical performance and sustainability of energy storage devices is durability. The cycling stability of PC//Al-CNC//PC supercapacitor was examined at a current density of 5 A $g^{-1}$ for 6 000 consecutive charge–discharge cycles (Fig. 6**e**). The flexible supercapacitor retained around 98.6% and 92% of the initial capacitance after 2 500 and 6 000 cycles, respectively, representing that the PC//Al-CNC//PC possess ultrahigh stability and superior to previously reported flexible symmetric SC based on PC (**Table S5**). Furthermore, the Coulombic efficiency of the device was examined and presented in Fig. 6**e**. The PC//Al-CNC//PC supercapacitor device possesses extraordinary Coulombic efficiency of around 99.9% after 6 000 consecutive charge–discharge cycles. To prove the electrochemical stability of the supercapacitor device, the GCD characteristics of the $10^{th}$ and 6 $000^{th}$ charge–discharge cycles are presented in the inset of Fig. 6**e**. No major changes were observed in the last GCD cycle, indicating the excellent electrochemical stability of PC and Al-CNC hydrogel. The energy and power densities of PC//Al-CNC//PC were calculated from the discharge curves and presented in the Ragone plot (Fig. 6**f**). The flexible supercapacitor achieved an energy density as high as 18.2 Wh $kg^{-1}$ at power density of 1 425 W $kg^{-1}$. Even at higher power densities of 20 833 W $kg^{-1}$, the device retained an energy density of 7.1 Wh $kg^{-1}$. The specific capacitance and cyclic stability showed superior energy and power densities compared to AC//Al-CNC//AC supercapacitor (3 Wh $kg^{-1}$ at power density of 40 W $kg^{-1}$) as well as previously reported flexible symmetric SC based on biowaste-derived PC (Fig. 6**f** and **Table S5**). To further validate the relevance of PC//Al-CNC//PC supercapacitor and illustrate its applicability, three devices were connected in series to power a red-light emitting diode (LED), as demonstrated in the inset of Fig. 6**f**.

Flexibility is one the significant aspects of energy storage devices and electronics, essential requirement for instance for wearables. The flexibility of PC//Al-CNC//PC supercapacitor was examined by using fresh

cells (**Figure S7**). The cells were analyzed by CV, GCD, EIS at different bending angles (0°, 90°, and 0° after bending) as shown in Fig. 7**a**. Fig. 7**a** depicts the CV curves at different bending angles at a constant scan rate of 50 mV $s^{-1}$. All CV curves show the same behavior with negligible capacitance degradation after straightening the device. Both GCD and EIS analyses are in good agreement with the CV results, in which the cells show no significant changes at different bending angles (Fig. 7**b and c**) confirming the high mechanical stability of the device (PC//Al-CNC//PC). At a bending angle of 90°, the calculated specific capacitance of the device showed an insignificant increase of < 0.1% compared to before and after bending (Fig. 7**b**). These results could be due to the reduction in the electrolyte thickness, which reduces the ion-transport pathway hence improving the ionic conductivity. Moreover, based on the fitted EC model (inset in Fig. 7**c**) and the obtained values (**Table S6**), the double layer capacity (CPE2-T) increased at bending angle of 90° compared to after bending, which is in good agreement with the aforementioned hypothesis. The obtained values for EC model showed that $R_b$ of the cells decreased by 0.198 Ω at 90° and after straightening the cell this value increased to 9.011 Ω (0.558 Ω higher than first cycle value). The double layer capacity of the cell was also increased at 90° and then decreased after straightening the cell. The results indicate that all-biowaste-derived SC can achieve outstanding overall electrochemical performance apart from their low-cost, facile process, non-toxic, and environmentally friendly. Therefore, bone-derived PC and Al-CNC hydrogel electrolyte have non-toxic nature which increases the potential of these renewable SC in wearable electronics.

## 4. Conclusion

In summary, we have successfully developed a flexible supercapacitor from biowastes, from brewery and animal bone residues, which were assembled as the Al-CNC hydrogel and PC components, respectively. The hydrogel electrolyte (Al-CNC) exhibited ultrahigh ionic conductivity of 24.9 mS $cm^{-1}$, high transmittance at a wavelength of 550 nm (~92.9%), and a maximum compression strength of 3.9 MPa. The bone-derived PC possesses outstanding specific capacitance (804 F $g^{-1}$ at 1 A $g^{-1}$), owing to its large specific surface area (~879 $m^2$ $g^{-1}$). Furthermore, the assembled PC//Al-CNC//PC flexible supercapacitor displayed high energy density (18.2 Wh $kg^{-1}$), exceptional power density (20 833 W $kg^{-1}$), and ultra-long cycle life of ~92% after 6 000 consecutive charge–discharge cycles. The developed supercapacitor maintained a high electrochemical performance at different bending angles. The results indicate the excellent prospects for biowaste-derived materials for next generation renewable flexible energy storage and conversion applications.

## Declaration of Competing Interest

The authors declare that they have no known competing financial interests or personal relationships that could have appeared to influence the work reported in this paper.

## Acknowledgments

Y. Al Haj and J. Vapaavuori acknowledge the generous funding from Academy of Finland's Flagship Programme under Projects No. 318890 and 318891 (Competence Center for Materials Bioeconomy, Finn-CERES). M. Borghei acknowledges Magnus Ehrnrooth foundation for supporting the CarboCat project. M. Borghei and O. Rojas acknowledge the European Union's Horizon 2020 research and innovation programme under grant agreement No 760876 (INNPAPER project) and the ERC Advanced Grant Agreement No. 788489 (BioElCell project). The Canada Excellence Research Chair initiative is gratefully acknowledged by O. Rojas. We acknowledge the provision of facilities by Aalto University at OtaNano - Nanomicroscopy Center (Aalto-NMC). T. Kallio acknowledge Business Finland the StoryEV (project 211780). T. Pääkkönen acknowledges the funding from Business Finland (R2B project: Gas-driven technology for cost-efficient production of cellulose nanocrystals 42472/31/2020).

## Appendix A. Supplementary data

Supplementary data to this article can be found online at https://doi.org/10.1016/j.cej.2022.135058.

## References

[1] X. Wang, X. Lu, B. Liu, D.i. Chen, Y. Tong, G. Shen, Flexible energy-storage devices: Design consideration and recent progress, Adv. Mater. 26 (28) (2014) 4763–4782, https://doi.org/10.1002/adma.201400910.
[2] J. Yang, Q. Cao, X. Tang, J. Du, T. Yu, X.i. Xu, D. Cai, C. Guan, W. Huang, 3D-Printed highly stretchable conducting polymer electrodes for flexible supercapacitors, J. Mater. Chem. A. 9 (35) (2021) 19649–19658.
[3] J. Pu, Q. Cao, Y. Gao, J. Yang, D. Cai, X. Chen, X. Tang, G. Fu, Z. Pan, C. Guan, Ultrafast-charging quasi-solid-state fiber-shaped zinc-ion hybrid supercapacitors with superior flexibility, J. Mater. Chem. A. 9 (32) (2021) 17292–17299.
[4] F. Béguin, V. Presser, A. Balducci, E. Frackowiak, Carbons and electrolytes for advanced supercapacitors, Adv. Mater. 26 (14) (2014) 2219–2251, https://doi.org/10.1002/adma.201304137.
[5] Y. Al Haj, J. Balamurugan, N.H. Kim, J.H. Lee, Nitrogen-doped graphene encapsulated cobalt iron sulfide as an advanced electrode for high-performance asymmetric supercapacitors, J. Mater. Chem. A. 7 (8) (2019) 3941–3952.
[6] A. Bahaa, J. Balamurugan, N.H. Kim, J.H. Lee, Metal-organic framework derived hierarchical copper cobalt sulfide nanosheet arrays for high-performance solid-state asymmetric supercapacitors, J. Mater. Chem. A. 7 (14) (2019) 8620–8632.
[7] M. Ue, M. Takeda, M. Takehara, S. Mori, Electrochemical Properties of Quaternary Ammonium Salts for Electrochemical Capacitors, J. Electrochem. Soc. 144 (8) (1997) 2684–2688, https://doi.org/10.1149/1.1837882.
[8] X. Peng, L. Peng, C. Wu, Y. Xie, Two dimensional nanomaterials for flexible supercapacitors, Chem. Soc. Rev. 43 (2014) 3303–3323, https://doi.org/10.1039/c3cs60407a.
[9] C. Meng, C. Liu, L. Chen, C. Hu, S. Fan, Highly flexible and all-solid-state paperlike polymer supercapacitors, Nano Lett. 10 (10) (2010) 4025–4031, https://doi.org/10.1021/nl1019672.
[10] X. Peng, H. Liu, Q. Yin, J. Wu, P. Chen, G. Zhang, G. Liu, C. Wu, Y. Xie, A zwitterionic gel electrolyte for efficient solid-state supercapacitors, Nat. Commun. 7 (2016) 1–8, https://doi.org/10.1038/ncomms11782.
[11] X.P. Morelle, W.R. Illeperuma, K. Tian, R. Bai, Z. Suo, J.J. Vlassak, Highly Stretchable and Tough Hydrogels below Water Freezing Temperature, Adv. Mater. 30 (35) (2018) 1801541, https://doi.org/10.1002/adma.201801541.
[12] L. Yang, L. Song, Y.i. Feng, M. Cao, P. Zhang, X.-F. Zhang, J. Yao, Zinc ion trapping in a cellulose hydrogel as a solid electrolyte for a safe and flexible supercapacitor, J. Mater. Chem. A. 8 (25) (2020) 12314–12318.
[13] X. Wang, C. Yao, F. Wang, Z. Li, Cellulose-Based Nanomaterials for Energy Applications, Small. 13 (42) (2017) 1702240, https://doi.org/10.1002/smll.201702240.
[14] S.-H. Wang, S.-S. Hou, P.-L. Kuo, H. Teng, Poly (ethylene oxide) -co-Poly (propylene oxide) -Based Gel Electrolyte with High Ionic Conductivity and Mechanical Integrity for Lithium- Ion Batteries, ACS Appl. Mater. Interfaces. 5 (17) (2013) 8477–8485.
[15] A. Pullanchiyodan, L. Manjakkal, S. Dervin, D. Shakthivel, R. Dahiya, Metal Coated Conductive Fabrics with Graphite Electrodes and Biocompatible Gel Electrolyte for Wearable Supercapacitors, Adv. Mater. Technol. 5 (5) (2020) 1901107, https://doi.org/10.1002/admt.201901107.
[16] J. Shojaeiarani, D. Bajwa, A. Shirzadifar, A review on cellulose nanocrystals as promising biocompounds for the synthesis of nanocomposite hydrogels, Carbohydr. Polym. 216 (2019) 247–259, https://doi.org/10.1016/j.carbpol.2019.04.033.
[17] H. Wang, J. Wu, J. Qiu, K. Zhang, J. Shao, L. Yan, In situ formation of a renewable cellulose hydrogel electrolyte for high-performance flexible all-solid-state asymmetric supercapacitors, Sustain, Energy Fuels. 3 (11) (2019) 3109–3115.
[18] X. Fu, W.-H. Zhong, Biomaterials for High-Energy Lithium-Based Batteries: Strategies, Challenges, and Perspectives, Adv. Energy Mater. 9 (40) (2019) 1901774, https://doi.org/10.1002/aenm.201901774.
[19] Z. Shi, X. Gao, M.W. Ullah, S. Li, Q. Wang, G. Yang, Electroconductive natural polymer-based hydrogels, Biomaterials. 111 (2016) 40–54, https://doi.org/10.1016/j.biomaterials.2016.09.020.
[20] B.L. Tardy, B.D. Mattos, C.G. Otoni, M. Beaumont, J. Majoinen, T. Kämäräinen, O. J. Rojas, Deconstruction and Reassembly of Renewable Polymers and Biocolloids into Next Generation Structured Materials, Chem. Rev. 121 (22) (2021) 14088–14188, https://doi.org/10.1021/acs.chemrev.0c0133310.1021/acs.chemrev.0c01333.s001.
[21] T. Pääkkönen, P. Spiliopoulos, Nonappa, K.S. Kontturi, P. Penttilä, M. Viljanen, K. Svedström, E. Kontturi, Sustainable High Yield Route to Cellulose Nanocrystals from Bacterial Cellulose, ACS Sustain, Chem. Eng. 7 (17) (2019) 14384–14388, https://doi.org/10.1021/acssuschemeng.9b0400510.1021/acssuschemeng.9b04005.s001.

[22] P. Spiliopoulos, S. Spirk, T. Pääkkönen, M. Viljanen, K. Svedström, L. Pitkänen, M. Awais, E. Kontturi, Visualizing Degradation of Cellulose Nanofibers by Acid Hydrolysis, Biomacromolecules. 22 (4) (2021) 1399–1405, https://doi.org/10.1021/acs.biomac.0c0162510.1021/acs.biomac.0c01625.s001.

[23] J. Peyre, T. Pääkkönen, M. Reza, E. Kontturi, Simultaneous preparation of cellulose nanocrystals and micron-sized porous colloidal particles of cellulose by TEMPO-mediated oxidation, Green Chem. 17 (2) (2015) 808–811.

[24] B. Ai, L. Zheng, W. Li, X. Zheng, Y. Yang, D. Xiao, J. Shi, Z. Sheng, Biodegradable Cellulose Film Prepared From Banana Pseudo-Stem Using an Ionic Liquid for Mango Preservation, Front, Plant Sci. 12 (2021) 1–10, https://doi.org/10.3389/fpls.2021.625878.

[25] H. Tibolla, F.M. Pelissari, F.C. Menegalli, Cellulose nanofibers produced from banana peel by chemical and enzymatic treatment, LWT - Food Sci. Technol. 59 (2) (2014) 1311–1318, https://doi.org/10.1016/j.lwt.2014.04.011.

[26] L. Cheng, X. Hu, Z. Gu, Y. Hong, Z. Li, C. Li, Characterization of physicochemical properties of cellulose from potato pulp and their effects on enzymatic hydrolysis by cellulase, Int. J. Biol. Macromol. 131 (2019) 564–571, https://doi.org/10.1016/j.ijbiomac.2019.02.164.

[27] M. Rajinipriya, M. Nagalakshmaiah, M. Robert, S. Elkoun, Importance of Agricultural and Industrial Waste in the Field of Nanocellulose and Recent Industrial Developments of Wood Based Nanocellulose: A Review, ACS Sustain. Chem. Eng. 6 (3) (2018) 2807–2828, https://doi.org/10.1021/acssuschemeng.7b03437.

[28] F. Kallel, F. Bettaieb, R. Khiari, A. García, J. Bras, S.E. Chaabouni, Isolation and structural characterization of cellulose nanocrystals extracted from garlic straw residues, Ind. Crops Prod. 87 (2016) 287–296, https://doi.org/10.1016/j.indcrop.2016.04.060.

[29] G. Siqueira, K. Oksman, S.K. Tadokoro, A.P. Mathew, Re-dispersible carrot nanofibers with high mechanical properties and reinforcing capacity for use in composite materials, Compos. Sci. Technol. 123 (2016) 49–56, https://doi.org/10.1016/j.compscitech.2015.12.001.

[30] T. Li, C. Chen, A.H. Brozena, J.Y. Zhu, L. Xu, C. Driemeier, J. Dai, O.J. Rojas, A. Isogai, L. Wågberg, L. Hu, Developing fibrillated cellulose as a sustainable technological material, Nature. 590 (7844) (2021) 47–56, https://doi.org/10.1038/s41586-020-03167-7.

[31] S.I. Mussatto, Brewer's spent grain: A valuable feedstock for industrial applications, J. Sci. Food Agric. 94 (7) (2014) 1264–1275, https://doi.org/10.1002/jsfa.6486.

[32] K. Rachwał, A. Waśko, K. Gustaw, M. Polak-Berecka, Utilization of brewery wastes in food industry, PeerJ. 8 (2020) 1–28, https://doi.org/10.7717/peerj.9427.

[33] Z. Wang, Y.-H. Lee, S.-W. Kim, J.-Y. Seo, S.-Y. Lee, L. Nyholm, Why Cellulose-Based Electrochemical Energy Storage Devices? Adv. Mater. 33 (28) (2021) 2000892, https://doi.org/10.1002/adma.202000892.

[34] A. Poosapati, E. Jang, D. Madan, N. Jang, L. Hu, Y. Lan, Cellulose hydrogel as a flexible gel electrolyte layer, MRS Commun. 9 (1) (2019) 122–128, https://doi.org/10.1557/mrc.2019.9.

[35] M. Chen, J. Chen, W. Zhou, J. Xu, C.-P. Wong, High-performance flexible and self-healable quasi-solid-state zinc-ion hybrid supercapacitor based on borax-crosslinked polyvinyl alcohol/nanocellulose hydrogel electrolyte, J. Mater. Chem. A. 7 (46) (2019) 26524–26532.

[36] M. Chau, S.E. Sriskandha, D. Pichugin, H. Thérien-Aubin, D. Nykypanchuk, G. Chauve, M. Méthot, J. Bouchard, O. Gang, E. Kumacheva, Ion-Mediated Gelation of Aqueous Suspensions of Cellulose Nanocrystals, Biomacromolecules. 16 (8) (2015) 2455–2462, https://doi.org/10.1021/acs.biomac.5b00701.

[37] H. Dong, J.F. Snyder, K.S. Williams, J.W. Andzelm, Cation-induced hydrogels of cellulose nanofibrils with tunable moduli, Biomacromolecules. 14 (9) (2013) 3338–3345, https://doi.org/10.1021/bm400993f.

[38] F. Ambroz, T.J. Macdonald, T. Nann, Trends in Aluminium-Based Intercalation Batteries, Adv. Energy Mater. 7 (15) (2017) 1602093, https://doi.org/10.1002/aenm.201602093.

[39] W. Pan, Y. Wang, Y. Zhang, H.Y.H. Kwok, M. Wu, X. Zhao, D.Y.C. Leung, A low-cost and dendrite-free rechargeable aluminium-ion battery with superior performance, J. Mater. Chem. A. 7 (29) (2019) 17420–17425.

[40] Y. Li, J. Fu, C. Zhong, T. Wu, Z. Chen, W. Hu, K. Amine, J. Lu, Recent Advances in Flexible Zinc-Based Rechargeable Batteries, Adv. Energy Mater. 9 (1) (2019) 1802605, https://doi.org/10.1002/aenm.201802605.

[41] K.J. De France, T. Hoare, E.D. Cranston, Review of Hydrogels and Aerogels Containing Nanocellulose, Chem. Mater. 29 (11) (2017) 4609–4631, https://doi.org/10.1021/acs.chemmater.7b00531.

[42] A. Borenstein, O. Hanna, R. Attias, S. Luski, T. Brousse, D. Aurbach, Carbon-based composite materials for supercapacitor electrodes: A review, J. Mater. Chem. A. 5 (25) (2017) 12653–12672.

[43] P. Yang, J. Xie, C. Zhong, Biowaste-Derived Three-Dimensional Porous Network Carbon and Bioseparator for High-Performance Asymmetric Supercapacitor, ACS Appl. Energy Mater. 1 (2) (2018) 616–622, https://doi.org/10.1021/acsaem.7b0015010.1021/acsaem.7b00150.s001.

[44] Y. Ji, Y. Deng, F. Chen, Z. Wang, Y. Lin, Z. Guan, Ultrathin Co3O4 nanosheets anchored on multi-heteroatom doped porous carbon derived from biowaste for high performance solid-state supercapacitor, Carbon N. Y. 156 (2020) 359–369, https://doi.org/10.1016/j.carbon.2019.09.064.

[45] G. Zhao, C. Chen, D. Yu, L. Sun, C. Yang, H. Zhang, Y. Sun, F. Besenbacher, M. Yu, One-step production of O-N-S co-doped three-dimensional hierarchical porous carbons for high-performance supercapacitors, Nano Energy. 47 (2018) 547–555, https://doi.org/10.1016/j.nanoen.2018.03.016.

[46] D. Yu, C. Chen, G. Zhao, L. Sun, B. Du, H. Zhang, Z. Li, Y.e. Sun, F. Besenbacher, M. Yu, Biowaste-Derived Hierarchical Porous Carbon Nanosheets for Ultrahigh Power Density Supercapacitors, ChemSusChem. 11 (10) (2018) 1678–1685, https://doi.org/10.1002/cssc.201800202.

[47] Y. Liu, Z. Xiao, Y. Liu, L.-Z. Fan, Biowaste-derived 3D honeycomb-like porous carbon with binary-heteroatom doping for high-performance flexible solid-state supercapacitors, J. Mater. Chem. A. 6 (1) (2018) 160–166.

[48] S. Liu, L. Wang, C. Zheng, Q. Chen, M. Feng, Y. Yu, Cost-Effective Asymmetric Supercapacitors Based on Nickel Cobalt Oxide Nanoarrays and Biowaste-Derived Porous Carbon Electrodes, ACS Sustain. Chem. Eng. 5 (11) (2017) 9903–9913, https://doi.org/10.1021/acssuschemeng.7b0186010.1021/acssuschemeng.7b01860.s001.

[49] L. Deng, Y. Zhang, Y. Wang, H. Yuan, Y. Chen, Y. Wu, In situ N-, P- and Ca-codoped biochar derived from animal bones to boost the electrocatalytic hydrogen evolution reaction, Resour. Conserv. Recycl. 170 (2021) 105568, https://doi.org/10.1016/j.resconrec.2021.105568.

[50] T. Pääkkönen, P. Spiliopoulos, A. Knuts, K. Nieminen, L.-S. Johansson, E. Enqvist, E. Kontturi, From vapour to gas: Optimising cellulose degradation with gaseous HCl, React, Chem. Eng. 3 (3) (2018) 312–318.

[51] T. Pääkkönen, C. Bertinetto, R. Pönni, G.K. Tummala, M. Nuopponen, T. Vuorinen, Rate-limiting steps in bromide-free TEMPO-mediated oxidation of cellulose - Quantification of the N-Oxoammonium cation by iodometric titration and UV-vis spectroscopy, Appl. Catal. A Gen. 505 (2015) 532–538, https://doi.org/10.1016/j.apcata.2015.07.024.

[52] N. Lin, C. Bruzzese, A. Dufresne, TEMPO-oxidized nanocellulose participating as crosslinking aid for alginate-based sponges, ACS Appl. Mater. Interfaces. 4 (9) (2012) 4948–4959, https://doi.org/10.1021/am301325r.

[53] S.S. Li, Y.L. Song, H.R. Yang, Q. Da An, Z.Y. Xiao, S.R. Zhai, Carboxymethyl cellulose-based cryogels for efficient heavy metal capture: Aluminum-mediated assembly process and sorption mechanism, Int. J. Biol. Macromol. 164 (2020) 3275–3286, https://doi.org/10.1016/j.ijbiomac.2020.08.186.

[54] W. Zhao, M. Jiang, W. Wang, S. Liu, W. Huang, Q. Zhao, Flexible Transparent Supercapacitors: Materials and Devices, Adv. Funct. Mater. 31 (11) (2021) 2009136, https://doi.org/10.1002/adfm.202009136.

[55] H.H. Rana, J.H. Park, G.S. Gund, H.S. Park, Highly conducting, extremely durable, phosphorylated cellulose-based ionogels for renewable flexible supercapacitors, Energy Storage Mater. 25 (2020) 70–75, https://doi.org/10.1016/j.ensm.2019.10.030.

[56] M. Borghei, N. Laocharoen, E. Kibena-Põldsepp, L.S. Johansson, J. Campbell, E. Kauppinen, K. Tammeveski, O.J. Rojas, Porous N, P-doped carbon from coconut shells with high electrocatalytic activity for oxygen reduction: Alternative to Pt-C for alkaline fuel cells, Appl. Catal. B Environ. 204 (2017) 394–402, https://doi.org/10.1016/j.apcatb.2016.11.029.

[57] L.-F. Chen, X.-D. Zhang, H.-W. Liang, M. Kong, Q.-F. Guan, P. Chen, Z.-Y. Wu, S.-H. Yu, Synthesis of Nitrogen-Doped Porous Carbon Nano fi bers as an E ffi cient Electrode Material for Supercapacitors, ACS Nano. 6 (8) (2012) 7092–7102.

[58] J. Niu, R. Shao, J. Liang, M. Dou, Z. Li, Y. Huang, F. Wang, Biomass-derived mesopore-dominant porous carbons with large specific surface area and high defect density as high performance electrode materials for Li-ion batteries and supercapacitors, Nano Energy. 36 (2017) 322–330, https://doi.org/10.1016/j.nanoen.2017.04.042.

[59] R. Wang, K. Wang, Z. Wang, H. Song, H. Wang, S. Ji, Pig bones derived N-doped carbon with multi-level pores as electrocatalyst for oxygen reduction, J. Power Sources. 297 (2015) 295–301, https://doi.org/10.1016/j.jpowsour.2015.07.107.

[60] H. Lei, J. Tu, D. Tian, S. Jiao, A nitrogen-doped graphene cathode for high-capacitance aluminum-ion hybrid supercapacitors, New J. Chem. 42 (19) (2018) 15684–15691, https://doi.org/10.1039/C8NJ02170H.

[61] A.K. Thakur, A.B. Deshmukh, R.B. Choudhary, I. Karbhal, M. Majumder, M. V. Shelke, Facile synthesis and electrochemical evaluation of PANI/CNT/MoS2 ternary composite as an electrode material for high performance supercapacitor, Mater. Sci. Eng. B Solid-State Mater. Adv. Technol. 223 (2017) 24–34, https://doi.org/10.1016/j.mseb.2017.05.001.

[62] Y. Guo, X. Zhou, Q. Tang, H. Bao, G. Wang, P. Saha, A self-healable and easily recyclable supramolecular hydrogel electrolyte for flexible supercapacitors, J. Mater. Chem. A. 4 (22) (2016) 8769–8776.

[63] S. Dong, X. He, H. Zhang, X. Xie, M. Yu, C. Yu, N. Xiao, J. Qiu, Surface modification of biomass-derived hard carbon by grafting porous carbon nanosheets for high-performance supercapacitors, J. Mater. Chem. A. 6 (33) (2018) 15954–15960.

[64] X. Lang, A. Hirata, T. Fujita, M. Chen, Nanoporous metal/oxide hybrid electrodes for electrochemical supercapacitors, Nat. Nanotechnol. 6 (4) (2011) 232–236, https://doi.org/10.1038/nnano.2011.13.

[65] J.J. Kaschuk, Y. Al Haj, O.J. Rojas, K. Miettunen, T. Abitbol, J. Vapaavuori, Plant-Based Structures as an Opportunity to Engineer Optical Functions in Next-Generation Light Management, Advanced Materials (2021), https://doi.org/10.1002/adma.202104473.